IEEE Access
Multidisciplinary | Rapid Review | Open Access Journal

Received March 30, 2021, accepted April 9, 2021, date of publication April 20, 2021, date of current version May 12, 2021.

Digital Object Identifier 10.1109/ACCESS.2021.3074458

Automated Microaneurysms Detection in Retinal Images Using Radon Transform and Supervised Learning: Application to Mass Screening of Diabetic Retinopathy

MEYSAM TAVAKOLI[1], ALIREZA MEHDIZADEH[2], AFSHIN AGHAYAN[3], REZA POURREZA SHAHRI[4], TIM ELLIS[5], AND JAMSHID DEHMESHKI[5,6]

[1]Department of Physics, Indiana University-Purdue University, Indianapolis, IN 46202, USA
[2]Department of Biomedical Physics and Engineering, Shiraz University of Medical Sciences, Shiraz 14336-71348, Iran
[3]Department of Geology, Boone Pickens School of Geology, Oklahoma State University, Stillwater, OK 74078, USA
[4]Department of Electrical Engineering, The University of Texas at Dallas, Richardson, TX 75080, USA
[5]Faculty of Science, Engineering, and Computing, Kingston University, London KT1 2EE, U.K.
[6]IAG, Image Analysis Group, London W6 8DL, U.K.

Corresponding author: Alireza Mehdizadeh (alireza.mehdizadeh@gmail.com and mehdizade@sums.ac.ir)

ABSTRACT Detection of red lesions in color retinal images is a critical step to prevent the development of vision loss and blindness associated with diabetic retinopathy (DR). Microaneurysms (MAs) are the most frequently observed and are usually the first lesions to appear as a consequence of DR. Therefore, their detection is necessary for mass screening of DR. However, detecting these lesions is a challenging task because of the low image contrast, and the wide variation of imaging conditions. Recently, the emergence of computer-aided diagnosis systems offers promising approaches to detect these lesions for diagnostic purposes. In this paper we focus on developing unsupervised and supervised techniques to cope intelligently with the MAs detection problem. In the first step, the retinal images are preprocessed to remove background variation in order to achieve a high level of accuracy in the detection. In the main processing step, important landmarks such as the optic nerve head and retinal vessels are detected and masked using the Radon transform (RT) and multi-overlapping windows. Finally, the MAs are detected and numbered by using a combination of RT and a supervised support vector machine classifier. The method was tested on three publicly available datasets and a local database comprising a total of 749 images. Detection performance was evaluated using sensitivity, specificity, and FROC analysis. From the image analysis viewpoint, DR was detected with a sensitivity of 100% and a specificity of 93% on average across all of these databases. Moreover, from lesion-based analysis the proposed approach detected the MAs with sensitivity of 95.7% with an average of 7 false positives per image. These results compare favourably with the best of the published results to date.

INDEX TERMS Diabetic retinopathy, supervised learning, microaneurysms, Radon transform, retinal image.

I. INTRODUCTION

Diabetic Retinopathy (DR) is a common complication of diabetes and the leading cause of blindness in the western countries [1]. It is a quiet disease and in the majority of cases identified by the patient when it is at the final stage where treatment is intricate and almost impossible. In general, the number of people afflicted by DR continues to grow at an alarming rate [2]. However, only half of the patients are aware of the disease. From statistical point of view, out of three diabetic individuals one of them has signs of DR [3]. Moreover, one out of ten tolerates DR severity and vision loss [4]. Therefore, annual examinations for all diabetic patients is strongly advised [5], [6]. If DR be detected at an early stage, its treatment can prevent loss of vision and blindness [7]. Thus, in order to diagnose diabetic people, screening

The associate editor coordinating the review of this manuscript and approving it for publication was Jenny Mahoney.

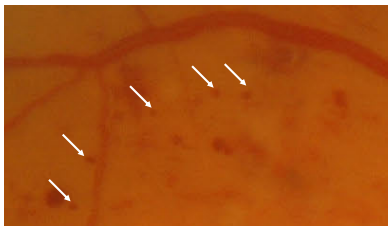

FIGURE 1. Sample MAs. A patch of single fundus image with different MAs. The arrows point MAs.

programs are currently in place around the world. It is believed that the DR screening of these people potentially reduces the risk of blindness to them by 50% [8].

However, regular screening requires immense costs, because of the large number of examinations. Moreover, there are not sufficient specialists especially in rural areas to perform so many examinations [9], [10]. Therefore, mass-screening of DR is not possible at present. Consequently, automated systems based on image processing approaches can help to overcome this problem by automatically detecting all retinal lesions in retinal images [11], [12], providing a more cost effective solution by screening retinal photographs. In this way, those patients who are diagnosed by the automated system would be referred to an ophthalmologist for further assessment. This would allow more patients to be screened per year allowing the ophthalmologists to spend more time on those patients who can get the most benefit from their expertise. In the same vein, automated screening systems are able to remove a large number of the individuals who do not have DR, reducing the workload of the ophthalmologists [13], [14]. In this way using Computer-Aided Diagnosis (CAD) systems [15], [16] which apply automated computerized techniques [17], can lead to rapid and appropriate detection [18], [19]. Such systems should be able to detect early signs of DR and provide an objective diagnosis based criteria defined by ophthalmologists.

The first signs of DR are Microaneurysms (MAs), tiny dilations of the capillaries, that can be seen at the first stage of DR [20]. Vision is not affected by MAs, but they are indicators for the progress of DR [21]. Hence, detection of MAs, which are visible directly after the arterial phase of fluorescein angiography [9], [11], is the first main step in the automated detection of DR. Furthermore, counting of MAs has been considered as a criteria for evaluation of the progress of the DR [11]. Fig. 1 shows examples of these lesions.

The aim of this study is to establish a system based on CAD which is suitable for mass screening of DR in color fundus images. Our primary focus and motivation in this study is to develop a fully automatic algorithm using a combination of unsupervised and supervised learning to detect red lesions (MAs) in retinal images, achieving a high level of sensitivity and specificity and minimising false responses. The first step uses an unsupervised method to detect potential candidates, followed by a support vector machine (SVM) to distinguish true MAs from false positives. This results in an increased sensitivity and decreased false positive rate per image derived from a limited number of training images compared with other supervised methods. Last but not least, the approach is benchmarked using several datasets that exhibit different resolutions and conditions (i.e. different types of DR).

The rest of the paper is organized as follows. The next section reviews other published studies in related area. Section III explains the proposed method for all retinal landmarks detection. Section IV introduces the material and databases used in this study. Section V presents the results and compares them to existing methods. The final section presents a discussion and conclusions.

II. PREVIOUS WORKS

There are several approaches for the automatic detection of MAs in color retinal images. These approaches can be generally classified into three groups which use morphological-based approaches, template matching, or supervised learning or some combination of each [9], [11], [22]–[36]. Similarly, some of these works aim for the automatic detection of DR [27], [28], [35], [36].

In [8] and [37] morphological algorithms are used to increase the detection accuracy for MAs. Although this type of analysis is typically fast and easy to apply, its simplicity can result in poor segmentation [30]. Morphological operations such as closing [9], and the top-hat transformation [11] have been used for the detection of MAs, tuned to their relatively uniform circular shape and limited size range. Wang *et al.* [25] used a dark object filtering process to locate candidates. Next, singular spectrum analysis was used to decompose cross-sectional profiles of extracted candidates. Finally, a kNN classifier and a set of statistical features of profiles were employed to distinguish the MAs from non-MAs. However, besides the above issue, most of the mathematical morphology methods mainly depend on the correct choice of structuring elements, and its benefits may be lost in tailoring their size and shape to match the range of MAs.

Another method utilizes template matching with multi-scale Gaussian kernels [24], [26], [29] because MAs approximate to a Gaussian-like peak in all projections and the intensity distribution of MAs is matched to a Gaussian distribution [24]. Therefore, template matching-based MA detection approaches have been proposed that can significantly increase the accuracy of MA detection. Using this idea, Quellec *et al.* applied a wavelet transform method for MAs detection. In their approach, they detected the MAs using local template matching in the wavelet domain [24]. Zhang *et al.* [26] used a multi-scale correlation coefficient based approach based on a non-linear filter with five Gaussian kernels at various standard deviations to detect MA candidates. Ram *et al.* [28] presented a feature based method that rejects specific classes of clutter whilst accepting a larger number of true MAs. The potential MAs that obtained after the final step were labeled with a grade that was based on their shape similarity to true MAs. Zhou *et al.* [33] introduced

an unsupervised classification method for MA detection that does not consider a non-MA training set. They used a new single statistic for distinguishing true MAs and non-MAs. As with the morphological approach, this type of algorithms still is limited due to its ignorance of hidden and unnoticeable structures. Moreover, it requires many parameters that are determined empirically.

A growing area is the application of machine learning [38] to MA detection using classification approaches are mostly seen recently [39]. Antal and Hajdu [40] applied a rule-based expert system for MAs detection. In this approach, after selection of MA candidates from retinal images, a rule-based classifier was applied to detect true MAs. Niemeijer *et al.* [22] used a strategy applying a combination of top-hat and supervised learning. In this approach, at first, MA candidates were selected using the method of Antal and Hajdu [40]; then a classifier was trained to differentiate true MAs from false ones. Although these machine learning approaches did well in detecting hidden structures of landmarks and MAs, they still depend on manually selected landmarks and empirically determined parameters [30]. Dashtbozorg *et al.* [23] detected MAs using gradient weighting and iterative thresholding. Local convergence index-based filters features were extracted and given to boosting classifier for classification of both MA and non-MAs. Similarly, Sanchez *et al.* [41] employed a mixture model-based clustering method for DR candidate extraction. Their method was followed by a logistic regression classifier to make a likelihood for each candidate based on its color, shape, and texture. Their proposed method for CAD was known to significantly reduce the time, cost, and effort of DR screening for large populations.

Deep learning based methods, [5], [30], [42]–[52] have been proposed and more specifically applied to automated DR detection [50]–[53]. Gulshan *et al.* [42] presented a supervised learning algorithm for automatically DR grading in retinal images. In this study, a deep neural network was applied to directly analyse the images and results of the DR grading. While this study addresses the issue of finding hidden structures and determining that empirical parameters are not needed, for training purpose the classifiers require a large number of retinal images and their manual interpretations, which is costly and time-consuming to create. Moreover, there are no quantitative results clearly produced for a certain MA. In fact for understanding and monitoring of the development of DR, these quantitative data are critical. Dai *et al.* [30] introduced a multi-sieving convolution neural network (CNN) framework integrating with the image-to-text mapping scheme for a guiding clinical report. They analyzed this clinical reports to get a probability map of MAs. Seoud *et al.* [5] proposed a novel method for automatic detection of MAs and haemorrhages in color retinal images. Their primary focus of study was a new set of shape landmarks, called Dynamic Shape Features, that did not need to precisely segment of red lesion regions. Haloi [54] implemented a deep learning network (five layers) with a dropout mechanism for diagnosing of early stage DR. A shortcoming of this approach was the requirement for a large amount of training data and computation time [55]. Using the approach introduced by Orlando *et al.* [45], they applied a 6-layer CNN model to segment the red lesions after extracting the candidates regions. However, as noted by Orlando, existing approaches rely heavily on hand-crafted features, which also require large annotated training databases with annotations. The reason is due to the deep learning needs large dataset, such that the feature learning is impossible. In fact, automatic feature learning is the most important advantage of deep learning, which has been well-known in the literature.

III. METHOD

A complete block diagram of the proposed method is presented in Fig. 2 and described in the following sections.

A. IMAGE PREPROCESSING

In the first step, before MAs and other landmarks can be investigated from a retinal image, the image needs to be preprocessed to ensure an acceptable level of accuracy in the detection. Generally, preprocessing is used to suppress information that is not appropriate to the image processing or analysis task including: color space conversion, retinal region detection, illumination equalization, and contrast enhancement. Initially, the color RGB image is transformed to the HSI color system. H is created from RGB values (normalized R, G, and B to range [0, 1]). In the next step (retinal region detection) the region of the retina is located in the HSI converted image, resulting in a binary image where the retina is labeled by 1's and the image background with 0's [56]. The masked retinal image is input to the third step, illumination equalization. This uses the original RGB image as input and equalizes inconsistent illumination over the retinal image [57]. This step results in a gray-level image using the green component of the original image, where the illumination has been equalized. In Contrast enhancement step by stretching the range of intensity values we attempted to improve the image quality [11]. Illumination equalization and contrast enhancement method are used to minimize inter-patient variation, which is a problem in the identification of retinal features due to the wide color variability of retinal images from different patients in the dataset. This variation mainly corresponds to different pigmentation and the iris color. In fact, without some color normalization, large changes in the original pigmentation of the retina can hamper discrimination of the comparatively small variation among the different characteristics. It is necessary to select a reference image and normalize the colors of all other retinal images in the dataset using a reference image. The color normalization is performed using histogram specification. This rectifies the image values through a histogram transformation operator which maps a given initial intensity distribution into a desired distribution using the histogram equalization technique [57], [58]. (See Fig. 3). The supplementary file provides more details of this step.

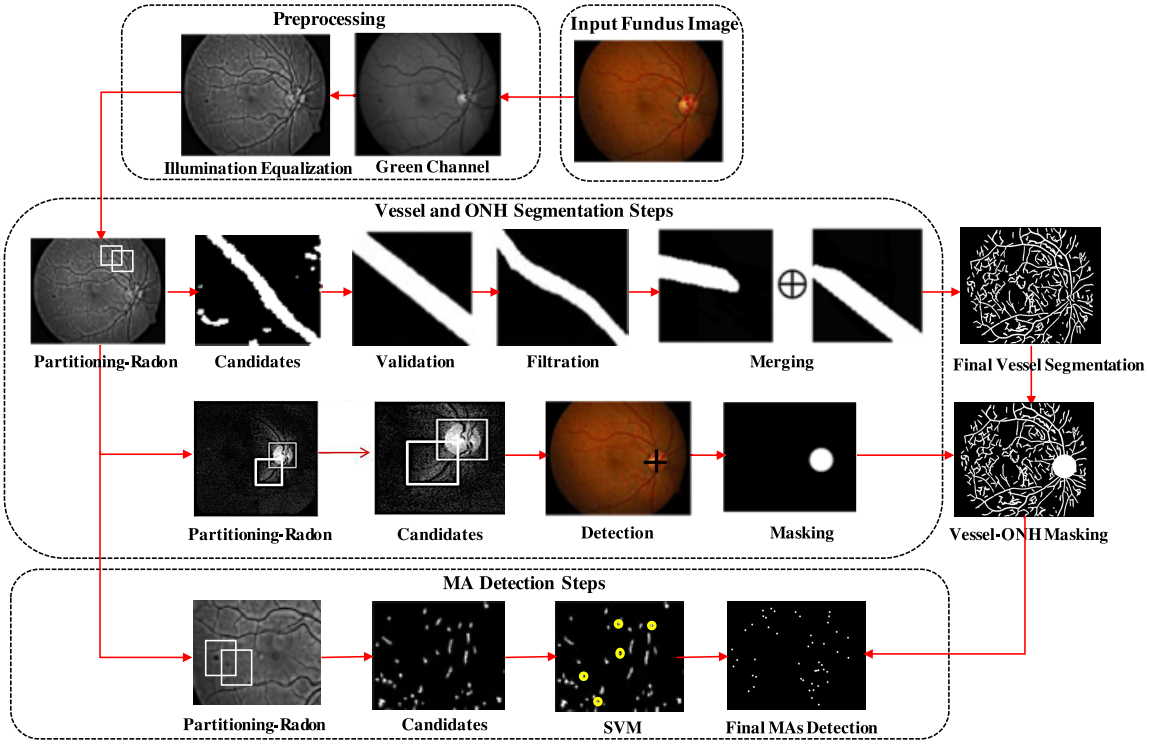

FIGURE 2. Graphical representation of processing steps.

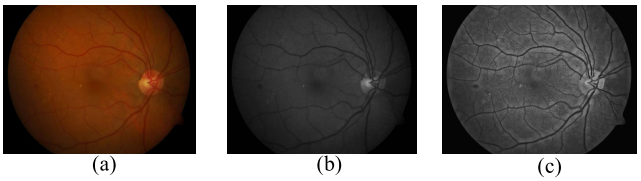

FIGURE 3. The preprocessing step. (a) Original RGB image (b) Original G channel (c) The preprocessing results.

B. MAIN PROCESSING

This step addresses the detection of other landmarks, vessels and the optic nerve head (ONH), and MAs using the preprocessed image. In the first step, vessels and the ONH are detected and masked from the preprocessed retinal image and this masked image will be used for the last step of MAs detection.

1) RETINAL VESSEL MASKING

The retinal blood vasculature is detected as dark curvilinear landmarks against a lighter background, with indistinct boarders. They are non-uniform in intensity, length and width throughout the image. As a result, global detection methods are prone to failure. Here, our approach works on the retinal image in local regions where the image characteristics are more homogeneous. The method is built in 4 steps: retinal image subdividing, Radon transform (RT), vessel validity, and vessel filtration. Further details involving the steps can be found in [59].

The following algorithms are applied to the preprocessed Green channel of retinal image which exhibits a higher contrast between the retinal blood vessels and the background is the reason for that. The image is firstly divided into some sub-windows. The size of each window ($n \times n$) is chosen to be at least twice the width of the thickest vessel in the image, which leads to a value for n that is approximately 2% of the full image width. A Local RT is then applied to each window. A problem with computing the local RT arises from the fact that as there more diagonal pixels in a rectangular window than the other directions, the Radon peak is more likely to appear in this diagonal direction. This issue can be addressed by applying a circular mask with the radius of half of the n to the preprocessed sub-image, as suggested by Tavakoli *et al.* [60]. To verify the vessel we compare the Radon peak amplitude of each sub-window with a prespecified threshold. The Radon peak of sub-windows in the Radon matrix would be indicative of a sub-vessel (i.e. if a vessel exists in the sub-window). If the peak amplitude is larger than the threshold, the detected vessel is confirmed, otherwise the next projection is analysed. This process is repeated for projections between 0 and π in increments of 6 degrees. The angle of projection that locates the peak is further processed to validate the existence of the vessel and calculate its width. Sub-windows of detected vessels are then combined to create a mask of the vascular tree, as shown in Fig. 4c. Here, because the vessels are segmented locally, based on an appropriate setting of the sub-window size (n), both thin and thick vessels

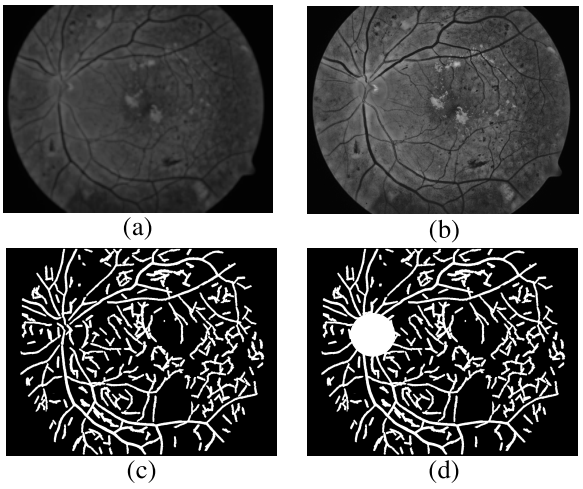

FIGURE 4. Masking process. (a) Original G channel image (b) Preprocessed image (c) Vessel segmentation and masking (d) Masking of the ONH and vessels.

are segmented. Another parameter in the algorithm is step size which determines the degree of overlap of the sub-windows. Fig. 5 shows the link between the step and window size. For more information refer to Tavakoli *et al.* [59], [60].

2) OPTIC NERVE HEAD MASKING

In general, large variation in the ONH contrast may result in artifact that is challenging for any retinal image analysis method. Therefore, it is critical to locate and mask the ONH. In the ONH detection step, because of this inhomogeneity the sub-windowing approach is effective. The algorithm uses 4 steps: Image partitioning, Local RT, ONH validation, and ONH masking [61].

The fundus image is initially divided into overlapping windows and a local RT is applied to each sub-window. Here, as in the vessel segmentation section, before applying the RT a circular mask is applied to minimize the effect of more pixels in the diagonal directions. Retinal structure is detected from above-threshold peaks in each sub-window. Detecting the ONH in candidate sub-windows exploits a property of the RT associated with circular patterns (Fig. 6). For a circular object, the RT has the same Radon profile at all angles. Because of the circularity of the ONH, all the projection profiles will have a high degree of similarity, which can be used to enable identification of the sub-window that contains the ONH. The boundary of the detected ONH is then refined. The algorithm's output is a circular mask located at the coordinates of the center of the sub-window. The radius of the mask is determined by the maximum possible radius of the ONH according to the resolution of the image. Masking the ONH ensures that it will be unable to interfere with the subsequent processing steps. The effect of masking is illustrated in Fig. 4d.

3) DETECTION OF MICROANEURYSMS

MAs are visible as small circular reddish patterns in color fundus images. They are specified by their diameter which is always smaller than $125\mu m$ [9]. Since MAs are isolated patterns, and disconnected from the retinal vessels, they tend to be of low contrast and are difficult to detect and separate from image noise or pigmentation changes. MAs are most visible in the preprocessed Green channel. Here, MA candidates are detected by means of the local RT. As described previously, the RT can be used to find a circular pattern in a window (see Fig. 6) because its integral characteristics make it less sensitive to image noise. In fact, the intensity fluctuations appear to have been removed in this case. Therefore, it can simultaneously be used to identify blood vessels (as linear patterns), and both the ONH and MAs (as circular patterns) in the retinal image. This is enabled by varying the window size (n), which is different for each pattern. Finally, a SVM classifier (a supervised classifier) is applied to separate true MAs from false candidates.

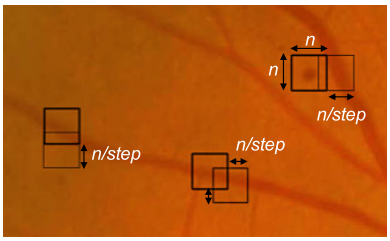

FIGURE 5. Multi-overlapping window step. The relation between window size (n) and overlapping step ratio.

a: SUBDIVIDING

MAs are detected using the described in the vessel and ONH detection steps, a window of size $n \times n$ is created which slides over the image (sub-windows). Choosing an appropriate window size results in the accurate detection of small or larger circular objects. According to the resolution of the image, the value of n is selected to be approximately 2% of the full image width which corresponds to the maximum diameter of a MA in a retinal image. Another element here is the ratio of sub-windows overlap. Without overlapped sub-windows the performance of MA detection falls. Therefore, in the presented approach a parameter step is exploited to define the adjoining ratio of sub-windows overlap.

b: LOCAL RADON TRANSFORM

In the proposed method, the inverted Green channel of preprocessed sub-windows is chosen for computing the local RT. This enables a MA to be associated with Radon peaks (higher intensity) in Radon space. The RT is defined as:

$$f(s,\theta) = \int_0^y \int_0^x f(x,y)\delta(s - xcos\theta - ysin\theta)dxdy \quad (1)$$

where $f(s,\theta)$ is the projection of image intensity, $f(x,y)$, at an angle θ, δ is the Dirac delta function, and $s = xcos\theta + ysin\theta$, is the distance from the origin to the line being integrated. Both x and y in Eq. 1 are equal to the window size, n. In our approach, in order to distinguish the effect of the background on the MA Radon peak amplitude, we multiply the mean of

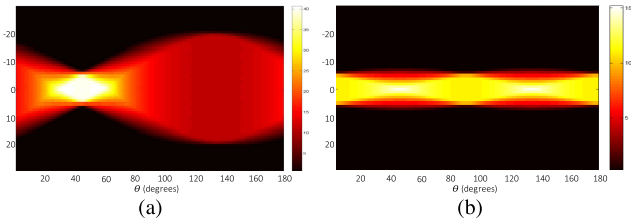

FIGURE 6. Illustration of Radon transform for a line and a point. (a) 2D illustration of Radon transform of a oblique line (45°) (b) 2D illustration of Radon transform of a point pattern in the center of sub-window.

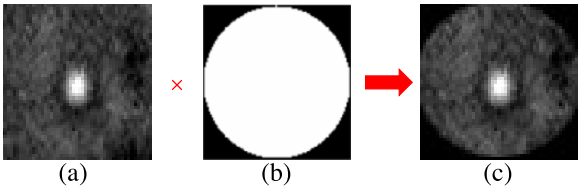

FIGURE 7. Sub-image masking process. (a) Green channel sub-image; (b) applied mask; (c) masked sub-image.

the sub-window by the window size (n) and the results is then subtracted from the projection profile. (Eq. 2)

$$R_{new} = \begin{cases} R_w - R_{mean}, & \text{if } (R_{sub-image} - R_{mean}) \geq 0 \\ 0, & else \end{cases} \quad (2)$$

R_{new} is the resulting RT from $R_{sub-image}$ which is the RT of the sub-image (or sub-window) and R_{mean}, the mean intensity image. Before starting the image subdividing lets look briefly at previous parts of this study in order to make the MA detection methods more accurate and robust.

To remove the diagonal effect on RT results, the input sub-window is masked by applying a circular mask. The result of masking procedure is shown in Fig. 7. The local RT is then applied to the masked image. As noted previously, a MA in a sub-window is related to peaks in Radon space; therefore, at this step Radon peaks should be identified. The sub-window, in which the peak occurs, is a candidate that might have a circular pattern. If for example a MA is located in the sub-window then peaks would be found in every column of Radon space, which means that at all Radon projection angles we should see a Gaussian pattern in each column, with a sharp peak in some rows. This profile is further processed for validation of candidate MA lesions.

c: VALIDATION

After applying the RT, the Radon matrix for each sub-window is created. In this matrix each column shows the line integral of a define projection angle. High intensity objects such as the ONH, sub-vessels, and MAs in the inverted green channel create a peak in Radon space. In the case of MA detection, an easy solution to validate MAs is to compare the Radon peak amplitude with pre-specified thresholds. The semi-circular pattern of a MA produced this peak (Gaussian peak) in all columns of the RT matrix, these Gaussian peaks

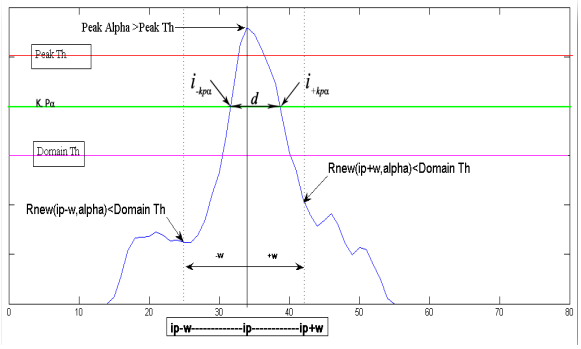

FIGURE 8. 2D illustration of Radon matrix. Normalized Radon matrix, R_{new}, of a sub-image from Fig. 7 R_{new} for projection angle of 35° and MA validation conditions demonstrated on it.

would have a similar pattern. Therefore, according to the maximum size and shape of a MA in the retinal image we definite two simple conditions to identify the peak forms in Radon space instead of fitting Gaussian function. The peak of every column (P_α) should be higher than the threshold (Peak Th), and the height of the peak pattern at a pre-specified distance (w) from its peak should be less than a second threshold (Domain Th). For more details see Fig. 8. These two conditions defined as Eq. 3 and are checked against R_{new}.

$$\begin{cases} 1 : P_\alpha \geq \text{Peak Th} \\ 2 : R_{new}(i_{P_\alpha} \pm w, \alpha), \leq \text{Domain Th} \end{cases} \quad (3)$$

$R_{new}(i_{P_\alpha} \pm w, \alpha)$ is used to show two Radon matrix elements in the same projection angle (α). If a MA exists in a sub-window these two conditions would be passed for all columns (projection angle), but this rarely occurs. All validated MA candidates were found in the form of some blocks, each one including only a MA candidate.

d: SUPERVISED LEARNING CLASSIFICATION

To decrease the number of false positives among valid candidates identified through the operations of the previous section, all candidates are classified into MA or non-MA categories. An MA should meet three criteria [9]: (i) according to retinal micro-vascular architecture, MAs only occur in capillaries, thus they are far from each other (more than 20 pixels in this case) and should never overlap; (ii) MAs should have a semi-circular shape; and (iii) MAs should be of uniform intensity. For the first criteria we check each 5 overlapped windows in all directions with their associated Radon profile and only one of them (with maximum and same profile in all directions) could remain and others would be filtered out. The result of this filtering process shows completely separate candidate blocks. To address the other two criteria a supervised learning process using a 2D vector for each validated candidate followed by a SVM classifier to distinguish true MAs from non-MAs (which are taken as false positive candidates) is applied. After considering alternative classification methods [62] (random forest and a neural network) SVM was selected as the best choice, and

follows the recommendations of previous researchers [63]. SVMs are a natural choice for two-class problems, and they demonstrate good performance in high dimensional spaces. The idea behind the SVM is to extract the hyper-plane that perfectly separates vectors from both classes in feature space while maximizing the distance from each class to the hyper-plane [64].

The following categories of features are used to distinguish true MAs from false positives:

- Binary features, such as size and shape of the MA candidates.
- Intensity-based features describing the gray level distribution the candidate regions.
- Color features in terms of the color within the MA candidate region.

The following define the actual features used:

(1) area (number of pixels of the candidate region);

(2) circularity measure ($\frac{perimeter^2}{4\pi Area^2}$);

(3) total intensity of the candidate region (in the green channel;

(4) mean intensity of the green channel;

(5) normalized intensity of the green channel;

(6) normalized mean intensity of the color values;

(7) mean value of the region surrounding the candidate region (green channel);

(8) standard deviation of the surrounding region;

(9) standard deviation of preprocessed sub-window;

(10) mean value of the associated closing of the preprocessed sub-window (to identify candidates situated on vessels);

(11) standard deviation value of the associated closing of the preprocessed sub-window; and

(12) the dynamical range of the preprocessed sub-window on the surroundings of the associated candidates.

The circularity of a candidate region is calculated from the variation in the MA diameter at different orientations, extracted from the projection columns in the Radon matrix of R_{new}.

To calculate the MA diameter in each sub-window, assume that the P_α (Fig. 8) is the peak in the α Column and the MA center located at i_p and K is a constant ($0 < K < 1$); points of height ($K \times P_\alpha$) are located either side of the peak, i.e. at (i_{+KP_α}) and (i_{-KP_α}) and the diameter would be equal to their difference.

$$\begin{aligned} R_{new}(i_{+KP_\alpha}) &= R_{new}(i_{-KP_\alpha}) = K \times P_\alpha \\ d_\alpha &= i_{+KP_\alpha} - i_{-KP_\alpha} \end{aligned} \tag{4}$$

The first dimension then would be calculated by variance of d_α according to different projection angle(α). Second dimension of vector is achieved by calculating the variance of peak (P_α) in different projection angle (α) of Radon matrix, R_{new}. In the final step the SVM would find a class of true MAs and algorithm eliminate other validated candidate. As we have shown in Fig. 9 a sample result, our approach extracts all MAs in all size well even either we have in low contrast regions or with very small diameter.

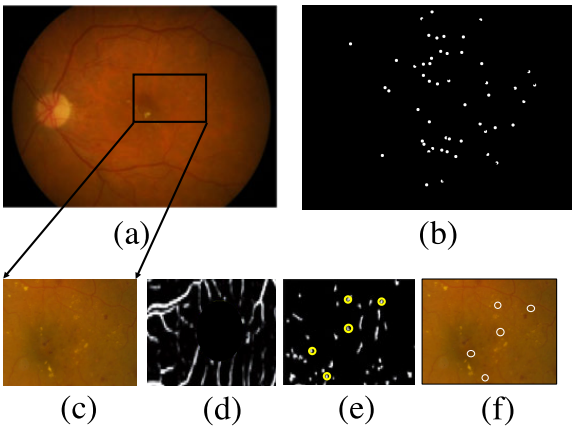

FIGURE 9. Result of MA detection. (a) Original image, (b) result of MA detection algorithm, (c) selected region of interest (ROI), (d) vessel masking of the ROI, (e) candidates of the ROI, (f) final MAs detection of the ROI.

IV. EXPERIMENTAL SETUPS

A. DATABASES

To benchmark the proposed MA detection method described in this study, four datasets (one local and three publicly available) were used (See Tables 1 and 2). The full dataset comprises a total of 749 images, with 95 normal fundus images (i.e. without MAs), and 654 images that have been classified by ophthalmologists with DR. Details of the individual datasets are as follows:

1- The first set (rural database) was named **MUMS-DB** (Mashhad University Medical Science Database). The MUMS-DB provided 220 retinal images including 200 cases with DR (with varying severity, mild, moderate and severe) and 20 without DR [61], [65]. The images were obtained via a TOPCON (TRC-50EX) retinal camera at 50 degree field of view (FOV) and mostly obtained from the posterior pole view (including ONH and macula) with a resolution of 2896×1944 pixels.

2- The second is the **DRIVE** database consisting of 40 images; 33 images have no signs of DR and 7 images showed signs of early or mild DR. For this set, two specialists provided manual segmentations for each image [66]. The images were captured using a Canon CR5 non-mydriatic 3CCD camera with a 45 degree FOV. Each image was taken using 8 bits per color plane at 768×584 pixels. Furthermore, a mask image is available for every retinal image, indicating the region of interest.

3- The **MESSIDOR** database consists of 400 undilated retinal images. For each image, a DR grade is provided as well as a risk of macular edema. In this study, we used only the DR grades, which are based on the number of MAs [67]. The images of the posterior pole were captured using a color video 3CCD camera mounted on a Topcon TRC NW6 non-mydriatic retinograph with a 45 degree FOV. Images were captured using 8 bits per color plane at 1440×960, 2240×1488 or 2304×1536 pixels.

TABLE 1. Details for image based analysis for all datasets in this study.

Database	Image Size	FOV	Normal	Abnormal	Sensitivity	Specificity	No. of Images
MUMS-DB [11]	2896 × 1944	50	20	200	100%	93%	220
DRIVE [66]	768 × 584	45	33	7	100%	96%	40
MESSIDOR [67]	1440 × 960	45	50	350	100%	91%	400
DIARETDB1 [68]	1500 × 1152	50	5	84	100%	90%	89

TABLE 2. Details for lesion based analysis for all datasets in this study [69].

Database	Total Red Lesions	**MAs**	Sensitivity	Specificity	F-Measure
MUMS-DB [11]	1847	1743	96.6%	95.12%	94.7%
DRIVE [66]	66	40	97.72%	94.23%	95.1%
MESSIDOR [67]	4072	3142	96.02%	96.89%	95.4%
DIARETDB1 [68]	714	440	96.7%	95.15%	95.9%

4- The **DIARETDB1** dataset includes 89 retinal images produced under different imaging settings; 84 images have symptoms of mild or pre-proliferative DR, and the rest are healthy images. Four different ophthalmologists have delineated the regions where MAs can be found [68]. Images were acquired using a 50 degree FOV digital fundus camera. Each image was taken using 8 bits per color plane at 1500 × 1152 pixels.

B. TRAINING AND TESTING DATABASES

To tune our parameter to achieve maximum accuracy and evaluate the effectiveness of a classification scheme a dataset is partitioned into training and testing subsets.

For the DRIVE dataset, the 20 of the hand-labeled segmentation images are used as the training set and the remaining 20 form the test set. The DIARETDB1 public database is divided into 28 training images and 61 testing images, each with the ground truth created by an expert ophthalmologist.

For the other two datasets (MESSIDOR and MUMSDB) there is no distinction between images that are used separately for training or test set. Hence, for the both datasets the classifier is evaluated using an iterated leave-one-out methodology [70], where the model is trained on 619 images and tested on the remaining one. The benefits of this method (compared with, say, random sampling [71]) is that the training and test images do not overlap and the network is trained on all the images in the dataset.

V. EXPERIMENTAL RESULTS

The aim of this study is to establish an automated screening method for identifying the DR by detecting MAs. Here, the focus is on detecting MAs as the most important vascular lesions to identify early stage DR from non-mydriatic color retinal images. Although patient analysis is more important, pixel-based analysis would give more information on accuracy of the algorithm presented here.

In Fig. 10, the accuracy of the diagnosis is assessed using ROC curve analysis, and concept of the sensitivity (or true positive rate (TPR)) and specificity (or 1−false positive rate(FPR)) measures. The ROC curve illustrates the tradeoff between sensitivity and specificity (Eq. 6) for a range of thresholds and enable the identification of an optimal value [65]. By varying the value of Peak *Th* (Eq. 3) in the interval [0, 1] the values for TPR and FRP are calculated and the ROC curve is plotted. However, different classification goals might make the selection of one point on the curve more appropriate for one task whilst another point may be more suitable for a different task. Hence, assessment using the ROC curve is a way to benchmark the model independent of the choice of threshold. The results for the automated method are compared to the groundtruth or gold standard (GS), which is manual detection by an expert ophthalmologist. Sensitivity and specificity are computed as:

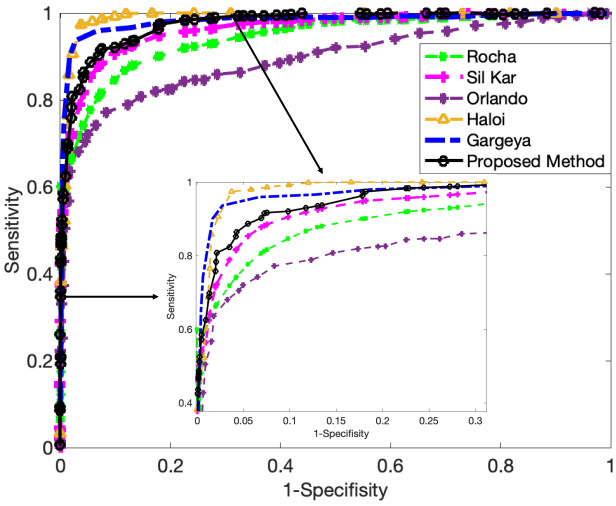

FIGURE 10. Comparison of ROC curves for DR detection approaches. Comparative analysis of ROC curves of the proposed method and related approaches [43], [45], [54], [69], [75] from the DIARETDB1 dataset.

$$TPR = Sensitivity = \frac{TP}{TP + FN}$$
$$FPR = 1 - Specificity = \frac{TN}{TN + FP} \quad (5)$$

where TP is a count of true positives, TN counts the true negatives, FP the false positives and FN the false negatives as in [72]. Moreover, the performance of MA detection is benchmarked separately by plotting the free-response operating characteristic (FROC) curve. As we have shown in Fig. 11, in FROC analysis the sensitivity of the algorithm is evaluated with respect to the average number of false positives per image. Additionally, the F-Measure [73], [74] is chosen to assess the accuracy of the proposed approach (See Table 2). The F-Measure value indicates the balance between the precision and the recall. All measures can be calculated from TP, FP, FN, and TN rates.

$$F - Measure = \frac{2Precision \times Recall}{Precision + Recall} \quad (6)$$

where the precision is computed by $\frac{TP}{TP+FP}$, and recall is calculated by $\frac{TP}{TP+FN}$.

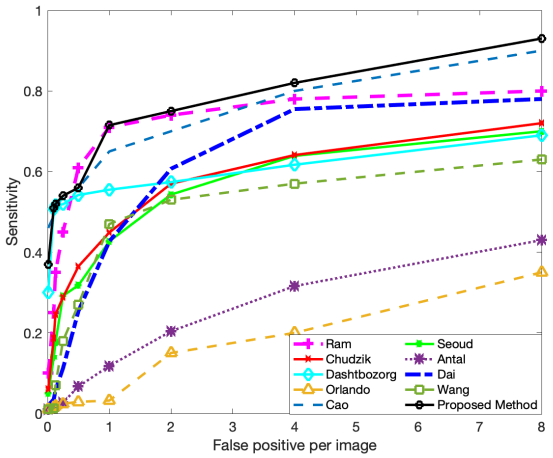

FIGURE 11. Comparison of FROC curves for MA detection approaches. Comparative study of FROC curves of the propose method with the state of the art approaches [5], [23], [25], [28], [30], [40], [45], [46], [63] using the DIARETDB1 dataset.

A. DETECTION OF VESSEL MAP

Small vessels may be detected from small isolated patterns, which could be identified as false positives in the detection of MAs. detection of MAs. The proposed method was initially used to segment the vessels in images from a fluorescein angiography database (Tavakoli *et al.* [59]). The algorithm is shown to have a sensitivity of more than 90% for vessel segmentation when applied to the images from the color databases used in this study. Retinal vessel detection is used to create a vessel map from the retina.

To investigate the effect of vascular detection and masking, a comparison was made between the results of MA detection with and without the removal of the vessels (Table 3). Without vessel masking the sensitivity remained unchanged at 100% in an image-based analysis; however, the specificity dropped from 93% with masking to 75% without it. From MA (lesion) based analysis view point, sensitivity increases from 95.7% to 99.5% without vessel masking; in addition, with masking the number of FP's per image decreases from 33.2 to 7.

B. DETECTION OF MICROANEURYSM

There are two different levels for an evaluation of the performance of MA detection: an image level and a lesion level analysis. In this section, we discuss both evaluation levels; firstly for image level analysis, where DR would be diagnosed when there are more than 5 MAs per image [11].

1) IMAGE BASED ANALYSIS

For the 749 images across all datasets, including 95 normal fundus images (without any MAs), and the rest DR images according to the final GS rating. The algorithm found 660 candidates with MAs, consisting of 654 true positive (TP) images that contained more than 5 MAs, and 6 false positive (FP) images. 89 out of 95 healthy fundus images were correctly detected as true negatives (TN), whilst no DR images were falsely diagnosed as healthy (FN). A diagnosis of DR according to MA detection in this stage is acceptable

TABLE 3. MA detection results in image based analysis with and without vessel removal.

-	Without	Vessel Removal	With	Vessel Removal
Database	Sensitivity	Specificity	Sensitivity	Specificity
MUMS-DB	100%	75%	100%	93%
DRIVE	100%	78%	100%	96%
MESSIDOR	100%	74%	100%	91%
DIARETDB1	100%	70%	100%	90%

and shows a sensitivity of 100% and a specificity of 93%. Table 3 shows a comparison of the performance of the proposed approach with and without removal of the vessel map. Whilst vessel removal has not affected the sensitivity of the algorithm to detect MAs, the specificity is significantly affected.

2) LESION BASED ANALYSIS

Here, it is informative to consider performance of MA detection for further MA analysis. A total of 5365 MAs were manually identified across the set of DR images; in the 95 normal images there were either zero MAs or less than 5 (in the case of six of the images); all the other images had more than 5 MAs [76]. The proposed method detected 5634 MAs across the full database of images; of these, 5241 were true positives (TP) associated with the diagnosed of diagnosed 5365 MAs, and only 124 MAs were missed (FN). 398 out of the 5634 MAs detected by the automated method were detected in the healthy tissue of the normal samples. Therefore, using Eq. 6 the sensitivity of the lesion based analysis is 95.7%. Calculating the specificity of the method in the pixel-based analysis requires, true negative value. The statistical value which could help us in evaluating the method is average false positives per image value; FP per image, which is 7.

VI. DISCUSSION

This study has presented and validated an algorithm to detect the MAs in a fully-automatic fashion. An important feature of the study is the use of the RT, as an unsupervised approach, to detect the all landmarks such as the vascular tree, ONH, and MAs in fundus images and also SVM, using supervised learning, to classify between MA and non-MA candidates associated with the low FP rate per image. Computers are effective at difficult tasks involving the production of quantitative information from images because their ability to process data is fast and efficient and they have high level of reproducibility [5]. Hence, an automated screening system would help to reduce the workload of well-paid specialists, enabling hospitals to use their resources in other critical tasks [57]. Meanwhile, it would be possible to screen more people and more often by applying these systems, since they are less expensive than manual screening.

The detection of the retinal vasculature tree can simplify detection of other features that are signs of disease, such as MAs, and other changes in the vascular network including

neovascularization. Thin vessels are visible as substitute of small isolated features, which might otherwise be identified as false positives in the detection of MAs. Vascular segmentation was the first step of the processing, enabling masking of the vascular structure. This step decreases the number of FPs in the final detection of MAs. The accuracy of final results was not found to depend highly on the accuracy of vessel masking but does decreases the number of FPs per image (Table 3). The specificity of the proposed method decreased when the algorithm is applied without vascular removal. However, sensitivity did not change from 100% in the image-based analysis. In the lesion-based analysis without vascular masking, sensitivity increased from 97.7% to 99.5%. In the first situation (with vascular removal) we have an average of 7 FPs per image while without vascular removal it increased to 33.2 FPs per image. The SVM classifier, which was trained using the leave-one-out method, was then used to correctly discriminate MAs from non-MAs. In order to select the optimal parameters, all of the training images were tested with different combination of parameters [89].

The detection of MAs used two different levels of evaluation: the image and lesion-based analysis. Image-based analysis considered all 749 images from the datasets, including 95 normal fundus images, and 654 DR images classified according to the final Gold standard. Diagnosis of DR from MA detection was excellent and showed sensitivity of 100% and specificity of 93%.

As we said before, in looking for a united program for mass screening of DR, it is important to have sufficient sensitivity. If we look at the entire study, the sensitivity of the image (or patient) based analysis of MAs is the most critical purpose of this study. The sensitivity of 100% makes our CAD trustable in diagnosis of DR. Although the sensitivity is 100%, according to current digital legislation and also medical council law, confirmation of a disease for all medical plans should be done by a physician and CAD should not make any plan within the current legislation and ethical regimen. Moreover, since we focused on the lesion based analysis, it is instructive to monitor how effective is the detection of MAs really is. The sensitivity of 95.7% in MA based analysis suggests the potential of the algorithm, even in treatment planning and follows-up. Another statistical analysis that assisted in benchmarking the approach was achieving an average of only 7 FPs per image which performed better than all unsupervised methods and most supervised ones such as [43], [54]. The results demonstrate that it is feasible to employ the algorithms to support clinicians in classifying retinal images into normal and diseased classes, and thus support them in their decision making.

According to the results of ROC (Fig. 10) and FROC (Fig. 11) curves analysis, the proposed approach is shown close or better results than unsupervised methods and some supervised ones reported in the literature. From the measurement of AUC our method performed better than almost all unsupesrvised methods. In the supervised methods, our approach was better than [5], [30], [40], [45], [78] (see Table 4). In terms of false positive per image, our approach performs better than most of the methods applied to the DIARETDB1 images and is comparable with [28] (See Fig. 11).

TABLE 4. Performance comparison results to other methods in MA detection.

Type	Methods	Sensitivity	Specificity	AUC
Supervised	Orlando et al. [45]	91.09%	50%	0.89
	Costa et al. [39]	94%	86%	0.93
	Seoud et al. [5]	94%	50%	0.90
	Dai et al. [30]	87.80%	96.10%	0.93
	Gargeya and Leng [43]	94%	98%	0.97
	Haloi [54]	97.01%	95.10%	0.96
	Antal and Hajdu [40]	91%	50%	0.87
	Quellec et al. [47]	96.31%	94%	0.94
	Gao et al. [51]	96.31%	94%	0.94
	Tavakoli et al. [77]	90%	85%	0.90
	Sanchez et al. [41]	92.20%	50%	0.87
	Roychowdhury et al. [78]	100%	53%	0.90
	Zhang et al. [79]	97.2%	95.6%	0.97
Unsupervised	Niemeijer et al. [22]	100%	87%	0.88
	Quellec et al. [24]	89.62%	-	0.92
	Ram et al. [28]	90.10%	90.23%	-
	Sil Kar and Maity [69]	95.23%	95.12%	0.94
	Figueiredo et al. [80]	93.45%	88.92%	-
	Wankhede and Khanchandani [81]	94.59%	83.33%	0.95
	Romero-Ora et al. [82]	84%	88.89%	0.87
	Saleh et al. [83]	84.31%	93.63%	-
	Rocha et al. [75]	90%	60%	-
	Jushi and Karule [84]	89.22%	91%	0.92
	Kang et al. [85]	91.94%	88.24%	0.93
	Derwin et al. [86]	90.2%	85.95%	0.89
	Selcuk and Alkan [87]	85.2%	82.5%	0.86
	Manjaramkar and Kokare [88]	88.09%	92.65%	-
-	**Proposed Method**	95.70%	95.46%	0.97

In general, although some of supervised approaches have better results in MA detection, they are dependent on the training data and also sensitive to false edges [90]. To test our approach using high resolution images, a new local database (MUMS-DB) was utilized that contained three times the number of images in the most widely-used public datasets. Although the performance on this database was lower than the other three public datasets (about 4% less), it still detected MAs with high sensitivity and AUC (greater than 92%). More importantly, since this database has DR of varying severity (mild, moderate and severe examples of NPDR) the effectiveness of the algorithm was demonstrated on a wider range of DR lesions. Our algorithm, unlike some methods, such as [90], [91] which consider small MAs close to the vasculature as a part of the vessel map, distinguishes between MAs and segmented vessels by using an appropriate window size, n, and an accurate reconstruction process. However, our approach has one limitation. From computational viewpoint, the average processing time per image for our method running on a PC with an Intel Corei3 CPU at 2.13 GHz and 2 GB of RAM was 4.5 minutes, which is likely to be high for portable DR screening systems of the future. The reason for this arises from the use of the RT in overlapping windows. Without overlapping windows the computational time is less than a

minute, which is more acceptable, but results in a drop in the accuracy of MA detection.

From the deep learning view point, there are some excellent studies, which are mentioned in the section II, with very good results [30], [43], [53], [54], [63]. Our results are comparable to those reported in [30], [43] but less than in [54]. However, a drawback with these methods is that they need a huge database for training purposes. Our future plan is to investigate the combination deep neural networks and N-shot learning [92], [93] with the methods used in this study to see if results can be further improved.

VII. CONCLUSION

One advantage of our algorithm is that, unlike other approaches, such as [90], [91], [94] which consider some MAs close to the retinal vessels as a part of the vessel map, by using a combination of RT, overlapping windows of a selective size, and SVM it can distinguish between MAs and segmented vessels by using an appropriate window size, n, and an accurate SVM classification process that concluded small FP rate per image in compare to most of published approaches. Other advantages in the processing including: accurate detection of the retinal vessel's location, determination of some parameters such as the width and length of vessels, even determining the location of vessel bifurcation, and localization of the ONH which can assist clinicians in analysing images later by registration schemes. Our algorithm also has some significant benefits in the detection of MAs in retinal images, including its robustness to noise, because of the integral nature of the Radon transform, acceptable performance in the detection of both thick and thin retinal vessels by the combined methods of RT and multi-overlapping windows, and last but not least, the approach is simple in comparison with other studies mentioned here.

ACKNOWLEDGMENT

The authors would like to thank J. J. Staal, E. Decenciere, T Kauppi and their colleagues, for making their databases publicly available.

REFERENCES

[1] R. Lee, T. Y. Wong, and C. Sabanayagam, "Epidemiology of diabetic retinopathy, diabetic macular edema and related vision loss," *Eye Vis.*, vol. 2, no. 1, p. 17, Dec. 2015.

[2] R. L. Thomas, F. D. Dunstan, S. D. Luzio, S. R. Chowdhury, R. V. North, S. L. Hale, R. L. Gibbins, and D. R. Owens, "Prevalence of diabetic retinopathy within a national diabetic retinopathy screening service," *Brit. J. Ophthalmol.*, vol. 99, no. 1, pp. 64–68, Jan. 2015.

[3] J. Ding and T. Y. Wong, "Current epidemiology of diabetic retinopathy and diabetic macular edema," *Current Diabetes Rep.*, vol. 12, no. 4, pp. 346–354, Aug. 2012.

[4] J. W. Yau , S. L. Rogers, R. Kawasaki, E. L. Lamoureux, J. W. Kowalski, T. Bek, S.-J. Chen, J. M. Dekker, A. Fletcher, J. Grauslund, and S. Haffner, "Global prevalence and major risk factors of diabetic retinopathy," *Diabetes Care*, vol. 35, no. 3, pp. 556–564, 2012.

[5] L. Seoud, T. Hurtut, J. Chelbi, F. Cheriet, and J. M. P. Langlois, "Red lesion detection using dynamic shape features for diabetic retinopathy screening," *IEEE Trans. Med. Imag.*, vol. 35, no. 4, pp. 1116–1126, Apr. 2016.

[6] J. Wang, Y. Bai, and B. Xia, "Feasibility of diagnosing both severity and features of diabetic retinopathy in fundus photography," *IEEE Access*, vol. 7, pp. 102589–102597, 2019.

[7] M. Niemeijer, B. van Ginneken, S. R. Russell, M. S. A. Suttorp-Schulten, and M. D. Abràmoff, "Automated detection and differentiation of drusen, exudates, and cotton-wool spots in digital color fundus photographs for diabetic retinopathy diagnosis," *Invest. Ophthalmol. Vis. Sci.*, vol. 48, no. 5, pp. 2260–2267, 2007.

[8] A. D. Fleming, S. Philip, K. A. Goatman, J. A. Olson, and P. F. Sharp, "Automated assessment of diabetic retinal image quality based on clarity and field definition," *Investigative Ophthalmol. Vis. Sci.*, vol. 47, no. 3, pp. 1120–1125, Mar. 2006.

[9] T. Walter, P. Massin, A. Erginay, R. Ordonez, C. Jeulin, and J.-C. Klein, "Automatic detection of microaneurysms in color fundus images," *Med. Image Anal.*, vol. 11, no. 6, pp. 555–566, Dec. 2007.

[10] M. Tavakoli, S. Jazani, and M. Nazar, "Automated detection of microaneurysms in color fundus images using deep learning with different preprocessing approaches," *Proc. SPIE*, vol. 11318, Mar. 2020, Art. no. 113180E.

[11] M. Tavakoli, R. P. Shahri, H. Pourreza, A. Mehdizadeh, T. Banaee, and M. H. B. Toosi, "A complementary method for automated detection of microaneurysms in fluorescein angiography fundus images to assess diabetic retinopathy," *Pattern Recognit.*, vol. 46, no. 10, pp. 2740–2753, Oct. 2013.

[12] Z. Yan, X. Yang, and K.-T. Cheng, "A three-stage deep learning model for accurate retinal vessel segmentation," *IEEE J. Biomed. Health Informat.*, vol. 23, no. 4, pp. 1427–1436, Jul. 2019.

[13] E. Soto-Pedre, A. Navea, S. Millan, M. C. Hernaez-Ortega, J. Morales, M. C. Desco, and P. Pérez, "Evaluation of automated image analysis software for the detection of diabetic retinopathy to reduce the ophthalmologists' workload," *Acta Ophthalmologica*, vol. 93, no. 1, pp. e52–e56, Feb. 2015.

[14] M. Tavakoli, M. Nazar, and A. Mehdizadeh, "The efficacy of microaneurysms detection with and without vessel segmentation in color retinal images," *Proc. SPIE*, vol. 11314, Mar. 2020, Art. no. 113143Y.

[15] M. R. K. Mookiah, U. R. Acharya, C. K. Chua, C. M. Lim, E. Y. K. Ng, and A. Laude, "Computer-aided diagnosis of diabetic retinopathy: A review," *Comput. Biol. Med.*, vol. 43, no. 12, pp. 2136–2155, 2013.

[16] A. M. Mendonca and A. Campilho, "Segmentation of retinal blood vessels by combining the detection of centerlines and morphological reconstruction," *IEEE Trans. Med. Imag.*, vol. 25, no. 9, pp. 1200–1213, Sep. 2006.

[17] Y. He, W. Jiao, Y. Shi, J. Lian, B. Zhao, W. Zou, Y. Zhu, and Y. Zheng, "Segmenting diabetic retinopathy lesions in multispectral images using low-dimensional spatial-spectral matrix representation," *IEEE J. Biomed. Health Informat.*, vol. 24, no. 2, pp. 493–502, Feb. 2020.

[18] R. A. Welikala, J. Dehmeshki, A. Hoppe, V. Tah, S. Mann, T. H. Williamson, and S. A. Barman, "Automated detection of proliferative diabetic retinopathy using a modified line operator and dual classification," *Comput. Methods Programs Biomed.*, vol. 114, no. 3, pp. 247–261, May 2014.

[19] R. A. Welikala, M. M. Fraz, J. Dehmeshki, A. Hoppe, V. Tah, S. Mann, T. H. Williamson, and S. A. Barman, "Genetic algorithm based feature selection combined with dual classification for the automated detection of proliferative diabetic retinopathy," *Comput. Med. Imag. Graph.*, vol. 43, pp. 64–77, Jul. 2015.

[20] J. Xu, X. Zhang, H. Chen, J. Li, J. Zhang, L. Shao, and G. Wang, "Automatic analysis of microaneurysms turnover to diagnose the progression of diabetic retinopathy," *IEEE Access*, vol. 6, pp. 9632–9642, 2018.

[21] M. D. Abrámoff, M. Niemeijer, M. S. A. Suttorp-Schulten, M. A. Viergever, S. R. Russell, and B. van Ginneken, "Evaluation of a system for automatic detection of diabetic retinopathy from color fundus photographs in a large population of patients with diabetes," *Diabetes Care*, vol. 31, no. 2, pp. 193–198, Feb. 2008.

[22] M. Niemeijer, B. van Ginneken, J. Staal, M. S. A. Suttorp-Schulten, and M. D. Abramoff, "Automatic detection of red lesions in digital color fundus photographs," *IEEE Trans. Med. Imag.*, vol. 24, no. 5, pp. 584–592, May 2005.

[23] B. Dashtbozorg, J. Zhang, F. Huang, and B. M. ter Haar Romeny, "Retinal microaneurysms detection using local convergence index features," *IEEE Trans. Image Process.*, vol. 27, no. 7, pp. 3300–3315, Jul. 2018.

[24] G. Quellec, M. Lamard, P. M. Josselin, G. Cazuguel, B. Cochener, and C. Roux, "Optimal wavelet transform for the detection of microaneurysms in retina photographs," *IEEE Trans. Med. Imag.*, vol. 27, no. 9, pp. 1230–1241, Sep. 2008.

[25] S. Wang, H. L. Tang, L. I. A. Turk, Y. Hu, S. Sanei, G. M. Saleh, and T. Peto, "Localizing microaneurysms in fundus images through singular spectrum analysis," *IEEE Trans. Biomed. Eng.*, vol. 64, no. 5, pp. 990–1002, May 2017.

[26] B. Zhang, X. Wu, J. You, Q. Li, and F. Karray, "Detection of microaneurysms using multi-scale correlation coefficients," *Pattern Recognit.*, vol. 43, no. 6, pp. 2237–2248, Jun. 2010.

[27] M. E. Gegundez-Arias, D. Marin, B. Ponte, F. Alvarez, J. Garrido, C. Ortega, M. J. Vasallo, and J. M. Bravo, "A tool for automated diabetic retinopathy pre-screening based on retinal image computer analysis," *Comput. Biol. Med.*, vol. 88, pp. 100–109, Sep. 2017.

[28] K. Ram, G. D. Joshi, and J. Sivaswamy, "A successive clutter-rejection-based approach for early detection of diabetic retinopathy," *IEEE Trans. Biomed. Eng.*, vol. 58, no. 3, pp. 664–673, Mar. 2011.

[29] I. Lazar and A. Hajdu, "Retinal microaneurysm detection through local rotating cross-section profile analysis," *IEEE Trans. Med. Imag.*, vol. 32, no. 2, pp. 400–407, Feb. 2013.

[30] L. Dai, R. Fang, H. Li, X. Hou, B. Sheng, Q. Wu, and W. Jia, "Clinical report guided retinal microaneurysm detection with multi-sieving deep learning," *IEEE Trans. Med. Imag.*, vol. 37, no. 5, pp. 1149–1161, May 2018.

[31] C. Playout, R. Duval, and F. Cheriet, "A novel weakly supervised multitask architecture for retinal lesions segmentation on fundus images," *IEEE Trans. Med. Imag.*, vol. 38, no. 10, pp. 2434–2444, Oct. 2019.

[32] M. U. Akram, S. Khalid, A. Tariq, S. A. Khan, and F. Azam, "Detection and classification of retinal lesions for grading of diabetic retinopathy," *Comput. Biol. Med.*, vol. 45, pp. 161–171, Feb. 2014.

[33] W. Zhou, C. Wu, D. Chen, Y. Yi, and W. Du, "Automatic microaneurysm detection using the sparse principal component analysis-based unsupervised classification method," *IEEE Access*, vol. 5, pp. 2563–2572, 2017.

[34] U. M. Akram and S. A. Khan, "Automated detection of dark and bright lesions in retinal images for early detection of diabetic retinopathy," *J. Med. Syst.*, vol. 36, no. 5, pp. 3151–3162, Oct. 2012.

[35] D. Kumar, G. W. Taylor, and A. Wong, "Discovery radiomics with CLEAR-DR: Interpretable computer aided diagnosis of diabetic retinopathy," *IEEE Access*, vol. 7, pp. 25891–25896, 2019.

[36] Y. Sun and D. Zhang, "Diagnosis and analysis of diabetic retinopathy based on electronic health records," *IEEE Access*, vol. 7, pp. 86115–86120, 2019.

[37] M. Tavakoli, F. Kalantari, and A. Golestaneh, "Comparing different preprocessing methods in automated segmentation of retinal vasculature," in *Proc. IEEE Nucl. Sci. Symp. Med. Imag. Conf. (NSS/MIC)*, Oct. 2017, pp. 1–8.

[38] D. Ravì, C. Wong, F. Deligianni, M. Berthelot, J. Andreu-Perez, B. Lo, and G.-Z. Yang, "Deep learning for health informatics," *IEEE J. Biomed. Health Informat.*, vol. 21, no. 1, pp. 4–21, Jan. 2017.

[39] P. Costa, A. Galdran, A. Smailagic, and A. Campilho, "A weakly-supervised framework for interpretable diabetic retinopathy detection on retinal images," *IEEE Access*, vol. 6, pp. 18747–18758, 2018.

[40] B. Antal and A. Hajdu, "An ensemble-based system for microaneurysm detection and diabetic retinopathy grading," *IEEE Trans. Biomed. Eng.*, vol. 59, no. 6, pp. 1720–1726, Jun. 2012.

[41] C. I. Sánchez, M. Niemeijer, A. V. Dumitrescu, M. S. Suttorp-Schulten, M. D. Abràmoff, and B. van Ginneken, "Evaluation of a computer-aided diagnosis system for diabetic retinopathy screening on public data," *Investigative Ophthalmol. Vis. Sci.*, vol. 52, no. 7, pp. 4866–4871, Jun. 2011.

[42] V. Gulshan, L. Peng, M. Coram, M. C. Stumpe, D. Wu, A. Narayanaswamy, S. Venugopalan, K. Widner, T. Madams, J. Cuadros, and R. Kim, "Development and validation of a deep learning algorithm for detection of diabetic retinopathy in retinal fundus photographs," *J. Amer. Med. Assoc.*, vol. 316, no. 22, pp. 2402–2410, 2016.

[43] R. Gargeya and T. Leng, "Automated identification of diabetic retinopathy using deep learning," *Ophthalmology*, vol. 124, no. 7, pp. 962–969, Jul. 2017.

[44] M. D. Abràmoff, Y. Lou, A. Erginay, W. Clarida, R. Amelon, J. C. Folk, and M. Niemeijer, "Improved automated detection of diabetic retinopathy on a publicly available dataset through integration of deep learning," *Investigative Ophthalmol. Vis. Sci.*, vol. 57, no. 13, pp. 5200–5206, 2016.

[45] J. I. Orlando, E. Prokofyeva, M. del Fresno, and M. B. Blaschko, "An ensemble deep learning based approach for red lesion detection in fundus images," *Comput. Methods Programs Biomed.*, vol. 153, pp. 115–127, Jan. 2018.

[46] P. Chudzik, S. Majumdar, F. Calivá, B. Al-Diri, and A. Hunter, "Microaneurysm detection using fully convolutional neural networks," *Comput. Methods Programs Biomed.*, vol. 158, pp. 185–192, May 2018.

[47] G. Quellec, K. Charrière, Y. Boudi, B. Cochener, and M. Lamard, "Deep image mining for diabetic retinopathy screening," *Med. Image Anal.*, vol. 39, pp. 178–193, Jul. 2017.

[48] X. Zeng, H. Chen, Y. Luo, and W. Ye, "Automated diabetic retinopathy detection based on binocular siamese-like convolutional neural network," *IEEE Access*, vol. 7, pp. 30744–30753, 2019.

[49] S. Qummar, F. G. Khan, S. Shah, A. Khan, S. Shamshirband, Z. U. Rehman, I. A. Khan, and W. Jadoon, "A deep learning ensemble approach for diabetic retinopathy detection," *IEEE Access*, vol. 7, pp. 150530–150539, 2019.

[50] H. Pratt, F. Coenen, D. M. Broadbent, S. P. Harding, and Y. Zheng, "Convolutional neural networks for diabetic retinopathy," *Procedia Comput. Sci.*, vol. 90, pp. 200–205, Jan. 2016.

[51] Z. Gao, J. Li, J. Guo, Y. Chen, Z. Yi, and J. Zhong, "Diagnosis of diabetic retinopathy using deep neural networks," *IEEE Access*, vol. 7, pp. 3360–3370, 2019.

[52] Y. Sun, "The neural network of one-dimensional convolution—An example of the diagnosis of diabetic retinopathy," *IEEE Access*, vol. 7, pp. 69657–69666, 2019.

[53] J. Wang, Y. Bai, and B. Xia, "Simultaneous diagnosis of severity and features of diabetic retinopathy in fundus photography using deep learning," *IEEE J. Biomed. Health Informat.*, vol. 24, no. 12, pp. 3397–3407, Dec. 2020.

[54] M. Haloi, "Improved microaneurysm detection using deep neural networks," 2015, *arXiv:1505.04424*. [Online]. Available: https://arxiv.org/abs/1505.04424

[55] B. Wu, W. Zhu, F. Shi, S. Zhu, and X. Chen, "Automatic detection of microaneurysms in retinal fundus images," *Comput. Med. Imag. Graph.*, vol. 55, pp. 106–112, Jan. 2017.

[56] A. A.-H.-A.-R. Youssif, A. Z. Ghalwash, and A. A. S. A.-R. Ghoneim, "Optic disc detection from normalized digital fundus images by means of a vessels' direction matched filter," *IEEE Trans. Med. Imag.*, vol. 27, no. 1, pp. 11–18, Jan. 2008.

[57] M. Tavakoli, M. Nazar, and A. Mehdizadeh, "Effect of two different preprocessing steps in detection of optic nerve head in fundus images," *Proc. SPIE*, vol. 10134, Mar. 2017, Art. no. 101343A.

[58] R. C. Gonzalez, R. E. Woods, and S. L. Eddins, *Digital Image Processing Using MATLAB*. London, U.K.: Pearson, 2004.

[59] M. Tavakoli, A. R. Mehdizadeh, R. Pourreza, H. R. Pourreza, T. Banaee, and M. H. B. Toosi, "Radon transform technique for linear structures detection: Application to vessel detection in fluorescein angiography fundus images," in *Proc. IEEE Nucl. Sci. Symp. Conf. Rec.*, Oct. 2011, pp. 3051–3056.

[60] M. Tavakoli, A. Mehdizadeh, R. P. Shahri, and J. Dehmeshki, "Unsupervised automated retinal vessel segmentation based on Radon line detector and morphological reconstruction," *IET Image Process.*, pp. 1–15, 2021, doi: 10.1049/ipr2.12119.

[61] R. Pourreza-Shahri, M. Tavakoli, and N. Kehtarnavaz, "Computationally efficient optic nerve head detection in retinal fundus images," *Biomed. Signal Process. Control*, vol. 11, pp. 63–73, May 2014.

[62] M. Mohandes, M. Deriche, and S. O. Aliyu, "Classifiers combination techniques: A comprehensive review," *IEEE Access*, vol. 6, pp. 19626–19639, 2018.

[63] W. Cao, N. Czarnek, J. Shan, and L. Li, "Microaneurysm detection using principal component analysis and machine learning methods," *IEEE Trans. Nanobiosci.*, vol. 17, no. 3, pp. 191–198, Jul. 2018.

[64] L. N. Sharma, R. K. Tripathy, and S. Dandapat, "Multiscale energy and eigenspace approach to detection and localization of myocardial infarction," *IEEE Trans. Biomed. Eng.*, vol. 62, no. 7, pp. 1827–1837, Jul. 2015.

[65] M. Tavakoli, M. Nazar, A. Golestaneh, and F. Kalantari, "Automated optic nerve head detection based on different retinal vasculature segmentation methods and mathematical morphology," in *Proc. IEEE Nucl. Sci. Symp. Med. Imag. Conf. (NSS/MIC)*, Oct. 2017, pp. 1–7.

[66] M. Niemeijer, J. Staal, B. van Ginneken, M. Loog, and M. Abramoff, "Comparative study of retinal vessel segmentation methods on a new publicly available database," *Proc. SPIE*, vol. 5370, pp. 648–657, May 2004.

[67] E. Decencière, X. Zhang, G. Cazuguel, B. Lay, B. Cochener, C. Trone, P. Gain, R. Ordonez, P. Massin, A. Erginay, and B. Charton, "Feedback on a publicly distributed image database: The messidor database," *Image Anal. Stereol.*, vol. 33, no. 3, pp. 231–234, Aug. 2014.

[68] T. Kauppi, V. Kalesnykiene, J.-K. Kamarainen, L. Lensu, I. Sorri, A. Raninen, R. Voutilainen, H. Uusitalo, H. Kälviäinen, and J. Pietilä, "The DIARETDB1 diabetic retinopathy database and evaluation protocol," in *Proc. Brit. Mach. Vis. Conf.*, vol. 1, Sep. 2007, pp. 1–10.
[69] S. S. Kar and S. P. Maity, "Automatic detection of retinal lesions for screening of diabetic retinopathy," *IEEE Trans. Biomed. Eng.*, vol. 65, no. 3, pp. 608–618, Mar. 2018.
[70] J. Staal, M. D. Abramoff, M. Niemeijer, M. A. Viergever, and B. van Ginneken, "Ridge-based vessel segmentation in color images of the retina," *IEEE Trans. Med. Imag.*, vol. 23, no. 4, pp. 501–509, Apr. 2004.
[71] Q. Li, B. Feng, L. Xie, P. Liang, H. Zhang, and T. Wang, "A cross-modality learning approach for vessel segmentation in retinal images," *IEEE Trans. Med. Imag.*, vol. 35, no. 1, pp. 109–118, Jan. 2016.
[72] D. Marín, A. Aquino, M. E. Gegundez-Arias, and J. M. Bravo, "A new supervised method for blood vessel segmentation in retinal images by using gray-level and moment invariants-based features," *IEEE Trans. Med. Imag.*, vol. 30, no. 1, pp. 146–158, Jan. 2011.
[73] D. M. Powers, "Evaluation: From precision, recall and f-measure to ROC, informedness, markedness and correlation," 2011, *arXiv:2010.16061*. [Online]. Available: https://arxiv.org/abs/2010.16061
[74] J. Shan and L. Li, "A deep learning method for microaneurysm detection in fundus images," in *Proc. IEEE 1st Int. Conf. Connected Health, Appl., Syst. Eng. Technol. (CHASE)*, Jun. 2016, pp. 357–358.
[75] A. Rocha, T. Carvalho, H. F. Jelinek, S. Goldenstein, and J. Wainer, "Points of interest and visual dictionaries for automatic retinal lesion detection," *IEEE Trans. Biomed. Eng.*, vol. 59, no. 8, pp. 2244–2253, Aug. 2012.
[76] R. Pires, S. Avila, H. F. Jelinek, J. Wainer, E. Valle, and A. Rocha, "Beyond lesion-based diabetic retinopathy: A direct approach for referral," *IEEE J. Biomed. Health Informat.*, vol. 21, no. 1, pp. 193–200, Jan. 2017.
[77] M. Tavakoli and M. Nazar, "Comparison different vessel segmentation methods in automated microaneurysms detection in retinal images using convolutional neural networks," *Proc. SPIE*, vol. 11317, Feb. 2020, Art. no. 113171P.
[78] S. Roychowdhury, D. D. Koozekanani, and K. K. Parhi, "DREAM: Diabetic retinopathy analysis using machine learning," *IEEE J. Biomed. Health Informat.*, vol. 18, no. 5, pp. 1717–1728, Sep. 2014.
[79] X. Zhang, J. Wu, Z. Peng, and M. Meng, "SODNet: Small object detection using deconvolutional neural network," *IET Image Process.*, vol. 14, no. 8, pp. 1662–1669, Jun. 2020.
[80] I. N. Figueiredo, S. Kumar, C. M. Oliveira, J. D. Ramos, and B. Engquist, "Automated lesion detectors in retinal fundus images," *Comput. Biol. Med.*, vol. 66, pp. 47–65, Nov. 2015.
[81] P. R. Wankhede and K. B. Khanchandani, "Automated microaneurysms detection from retinal fundus images using pixel intensity rank transform," *Biomed. Pharmacol. J.*, vol. 13, no. 1, pp. 47–54, Mar. 2020.
[82] R. Romero-Oraá, J. Jiménez-García, M. García, M. I. López-Gálvez, J. Oraá-Pérez, and R. Hornero, "Entropy rate superpixel classification for automatic red lesion detection in fundus images," *Entropy*, vol. 21, no. 4, p. 417, Apr. 2019.
[83] M. D. Saleh and C. Eswaran, "An automated decision-support system for non-proliferative diabetic retinopathy disease based on MAs and HAs detection," *Comput. Methods Programs Biomed.*, vol. 108, no. 1, pp. 186–196, Oct. 2012.
[84] S. Joshi and P. Karule, "Mathematical morphology for microaneurysm detection in fundus images," *Eur. J. Ophthalmol.*, vol. 30, no. 5, pp. 1135–1142, Sep. 2019.
[85] Y. Kang, Y. Fang, and X. Lai, "Automatic detection of diabetic retinopathy with statistical method and Bayesian classifier," *J. Med. Imag. Health Informat.*, vol. 10, no. 5, pp. 1225–1233, May 2020.
[86] D. J. Derwin, S. T. Selvi, and O. J. Singh, "Discrimination of microaneurysm in color retinal images using texture descriptors," *Signal, Image Video Process.*, vol. 14, no. 2, pp. 369–376, Mar. 2020.
[87] T. Selçuk and A. Alkan, "Detection of microaneurysms using ant colony algorithm in the early diagnosis of diabetic retinopathy," *Med. Hypotheses*, vol. 129, Aug. 2019, Art. no. 109242.
[88] A. Manjaramkar and M. Kokare, "Statistical geometrical features for microaneurysm detection," *J. Digit. Imag.*, vol. 31, no. 2, pp. 224–234, Apr. 2018.
[89] M. Tavakoli, P. Kelley, M. Nazar, and F. Kalantari, "Automated fovea detection based on unsupervised retinal vessel segmentation method," in *Proc. IEEE Nucl. Sci. Symp. Med. Imag. Conf. (NSS/MIC)*, Oct. 2017, pp. 1–7.
[90] S. Roychowdhury, D. D. Koozekanani, and K. K. Parhi, "Iterative vessel segmentation of fundus images," *IEEE Trans. Biomed. Eng.*, vol. 62, no. 7, pp. 1738–1749, Jul. 2015.
[91] J. Zhang, B. Dashtbozorg, E. Bekkers, J. P. W. Pluim, R. Duits, and B. M. ter Haar Romeny, "Robust retinal vessel segmentation via locally adaptive derivative frames in orientation scores," *IEEE Trans. Med. Imag.*, vol. 35, no. 12, pp. 2631–2644, Dec. 2016.
[92] Y. Fu, T. M. Hospedales, T. Xiang, and S. Gong, "Transductive multi-view zero-shot learning," *IEEE Trans. Pattern Anal. Mach. Intell.*, vol. 37, no. 11, pp. 2332–2345, Nov. 2015.
[93] A. Naghizadeh, D. N. Metaxas, and D. Liu, "Greedy auto-augmentation for n-shot learning using deep neural networks," *Neural Netw.*, vol. 135, pp. 68–77, Mar. 2021.
[94] K. A. Vermeer, F. M. Vos, H. G. Lemij, and A. M. Vossepoel, "A model based method for retinal blood vessel detection," *Comput. Biol. Med.*, vol. 34, no. 3, pp. 209–219, Apr. 2004.